Materials Science & Engineering A 922 (2025) 147664

Contents lists available at ScienceDirect

Materials Science & Engineering A

journal homepage: www.elsevier.com/locate/msea

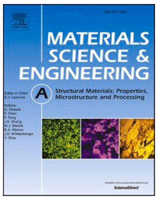

Gas tungsten arc welding of CoCrFeMnNi high entropy alloy to 316 stainless steel

Jiajia Shen [a,b,*], Rae Eon Kim [c], Jingjing He [d,e], J.G. Lopes [b], Jin Yang [f], Zhi Zeng [g], N. Schell [h], Hyoung Seop Kim [c,i], J.P. Oliveira [a,b]

[a] *CENIMAT/I3N, Department of Materials Science, NOVA School of Science and Technology, Universidade NOVA de Lisboa, 2829-516, Caparica, Portugal*
[b] *UNIDEMI, Department of Mechanical and Industrial Engineering, NOVA School of Science and Technology, Universidade NOVA de Lisboa, 2829-516, Caparica, Portugal*
[c] *Graduate Institute of Ferrous and Eco Materials Technology, POSTECH (Pohang University of Science and Technology), Pohang, 37673, South Korea*
[d] *Advanced Manufacturing Center, Ningbo Institute of Technology, Beihang University, Ningbo, 315800, China*
[e] *School of Reliability and Systems Engineering, Beihang University, Weimin Building, No. 37, Xueyuan Road, Haidian District, Beijing, China*
[f] *School of Materials Engineering, Shanghai University of Engineering Science, Shanghai, 201620, China*
[g] *School of Mechanical and Electrical Engineering, University of Electronic Science and Technology of China, Sichuan, 611731, China*
[h] *Institute of Materials Physics, Helmholtz-Zentrum Hereon, Max-Planck-Str. 1, 21502, Geesthacht, Germany*
[i] *Advanced Institute for Materials Research (WPI-AIMR), Tohoku University, Sendai, 980-8577, Japan*

ARTICLE INFO

Keywords:
Gas tungsten arc welding
CoCrFeMnNi high entropy alloys
316 stainless steel
Synchrotron X-ray diffraction
Mechanical testing

ABSTRACT

In this study, an as-annealed CoCrFeMnNi high entropy alloy (HEA) was successfully gas tungsten arc-welded (GTA-welded) to 316 stainless steel, resulting in a fully penetrated joint and free of visible macroscopic defects. In the heat-affected zone (HAZ) on the 316 stainless steel side, a phase transformation from δ-BCC to σ phase was detected. On the CoCrFeMnNi side, the base material (BM) primarily exhibited an FCC matrix phase, with a slight increase in Cr-Mn oxide content upon entering the HAZ. The formation of the BCC phase in the fusion zone (FZ) was mainly attributed to the mixing of Fe from the 316 stainless steel. This region exhibited the highest hardness, resulting from a combination of factors, including the BCC precipitates and minor incorporation of carbon introduced within the FZ, further aided by solid solution strengthening due to BMs mixing, but solid solution strengthening is the key factor. The BMs and the adjacent HAZs displayed highly similar equiaxed grain structure and size, and the hardness distributions, making it difficult to distinguish each region. However, the evolution of interplanar spacing obtained through synchrotron X-ray radiation effectively differentiated the various regions of the joint. Tensile testing revealed that the strength and hardness of this dissimilar joint were lower than those of both BMs, yet it still shows potential for structural applications. The fracture site of the joint occurred in the HAZ on the 316 stainless steel side, primarily due to the combined effects of localized large plastic deformation in the soft region and stress concentration caused by the presence of σ phase.

1. Introduction

In various manufacturing fields, 316 stainless steel has become the material of choice for constructing pipelines, containers, valves, and even critical components such as the magnetic coils in nuclear reactors [1–3]. This preference is attributed to its excellent corrosion resistance, superior mechanical strength, and stable processing characteristics [4,5]. However, with the rapid advancement of industrial technology and the continuous expansion of application areas, the performance requirements for materials have become increasingly stringent. The CoCrFeMnNi high-entropy alloy (HEA) [6,7], an innovative multi-component alloy system, has emerged as a promising candidate in engineering applications. This is due to its outstanding mechanical properties, including high strength, exceptional wear resistance, and excellent corrosion resistance under extreme conditions [8–10], making it a focal point of materials science research. Despite these significant performance advantages, the high cost and processing difficulties associated with HEAs have limited their widespread application. Therefore,

---

* Corresponding author. CENIMAT/I3N, Department of Materials Science, NOVA School of Science and Technology, Universidade NOVA de Lisboa, 2829-516 Caparica, Portugal.

E-mail addresses: j.shen@fct.unl.pt (J. Shen), jp.oliveira@fct.unl.pt (J.P. Oliveira).

https://doi.org/10.1016/j.msea.2024.147664
Received 4 October 2024; Received in revised form 22 November 2024; Accepted 9 December 2024

it is critical to explore effective methods for connecting HEAs with the relatively more affordable 316 stainless steel to achieve composite-like applications of dissimilar structural materials, thereby ensuring safety performance while reducing overall manufacturing costs. This challenge requires the development of reliable welding techniques to ensure a strong and durable connection between CoCrFeMnNi HEAs and 316 stainless steel [11,12].

Among various welding techniques, laser welding is highly regarded for its concentrated heat source [13,14]. However, despite the widespread recognition of laser welding's precision, its relatively high initial investment cost may limit broader application. In contrast, arc-based welding techniques, such as Gas Tungsten Arc Welding (GTAW), offer a more cost-effective alternative, while still enabling the production of high-quality joints under optimized process parameters. As a result, this study focuses on using an arc-based welding technique to explore the weldability of CoCrFeMnNi HEA to 316 stainless steel. During the arc-based welding process, the weld thermal cycle plays a crucial role in controlling both the solidification conditions and the potential solid-state transformations that may occur upon cooling from high temperature regimes in the heat affected zone (HAZ) and fusion zones (FZ). Specifically, for arc-based welding, key parameters such as the welding current (I), voltage (V), and travel speed (v) of the heat source, along with energy efficiency (η), are the primary parameters determining the heat input (HI), that is provided to the material to be welded. Here, it is worth mention that the h of arc-based welding is relatively low, ranging from 30 to 50 %, depending on the specific welding process. The HI is a fundamental parameter in fusion welding and is defined as $HI = \left(\frac{U \times I}{V}\right) \times \eta$. By adjusting the U, I, and v appropriately, it is possible to ensure sufficient HI during the welding, allowing the base material (BM) to melt and form a stable FZ. Optimizing welding parameters can help minimize potential defects such as lack of fusion, porosity, and cracks. Moreover, a stable welding process can also reduce the occurrence of cracks, thereby ensuring the quality of the welded joint. Typically, reducing HI is a key objective, as higher heat input leads to a larger extension of the thermally HAZ and FZ, and the microstructural changes induced by the weld thermal cycle can become more pronounced. Closely related to HI is the cooling rate: higher HI results in slower cooling rates across the welded joint. Therefore, the correct selection of HI during fusion-based welding process is essential for controlling both the microstructural evolution and the magnitude of residual stresses.

From welding metallurgy perspective, forming welded joints between HEAs and stainless steel presents significant challenges. During welding, the base materials (BMs) rapidly melt within the fusion zone (FZ), undergoing complex melting and non-equilibrium solidification processes. This leads to localized compositional complexity, which may induce the formation of brittle phases or intermetallic compounds, potentially compromising the mechanical properties of the joint. Therefore, it is crucial to systematically understand the microstructural evolution and mechanical performance of dissimilar joints. Here, in terms of application fields, welded joints of CoCrFeMnNi high-entropy alloy and 316 stainless steel have broad prospects in industries such as aerospace, petrochemical, and marine engineering. These industries require materials with high resistance to temperature, pressure, and corrosion, and welded joints can fully utilize the performance advantages of both materials to create composite-like structures with distinct characteristics, thus meeting the demands of extreme operating environments. For instance, in the aerospace industry, such welded joints can be used to manufacture critical components as engine parts and fuel systems; in the petrochemical industry, they can be applied in the production of high-pressure vessels, pipelines, and other key equipment; in marine engineering, they can be used to construct corrosion-resistant hulls and offshore platform infrastructures.

Although previous studies have confirmed the weldability of CoCrFeMnNi HEA [15–23], research on its weldability with other conventional alloys is still in its early stages [24–41] and has primarily focused on laser welding [27,31,33,36–39,41]. To the best of the author's knowledge, only one study has used gas tungsten arc welding [24] to investigate the weldability of CoCrFeMnNi with traditional alloys. So far, there has not yet been a systematic study on the weldability of CoCrFeMnNi with 316 stainless steels under arc-based welding conditions. Therefore, the results of this study fill a gap in the understanding of the compatibility between these two materials.

In this study, GTAW was selected to join CoCrFeMnNi HEA and 316 stainless steel. After welding, the microstructural evolution of the weld joint, influenced by the weld thermal cycle, was systematically analyzed using various multiscale techniques. These included optical microscopy, scanning electron microscopy combined with electron backscatter diffraction, high-energy synchrotron X-ray diffraction, and thermodynamic calculations. Additionally, the mechanical properties of the joint were comprehensively evaluated through microhardness and tensile testing. Based on these analyses, the present work elucidates the intrinsic relationship between the weld thermal cycle, microstructural evolution, and mechanical properties, providing essential theoretical foundations and technical support for the development of structural applications based on these two materials.

2. Experimental procedure

2.1. Sample preparation

In this study, both BMs used for dissimilar welding were in an annealed state, with the primary goal of ensuring optimal microstructural uniformity during the dissimilar welding process between CoCrFeMnNi HEA and 316 stainless steel, thereby improving the ductility of the joint. The equiatomic CoCrFeMnNi HEA was self-prepared following a three-stage process. First, the alloy ingot was produced by induction melting to ensure a homogeneous composition. Next, the alloy underwent cold rolling at room temperature, achieving a 50 % reduction in thickness (from 3 mm to 1.5 mm). Finally, high-temperature annealing was performed at 800 °C for 1 h under argon protection to eliminate rolling defects. The other BM, commercial 316 stainless steel, was sourced from MLGLnox and subjected to a specific heat treatment process: rapid annealing at 1050 °C for 1 min followed by immediate water quenching. The materials were then cut into 40 × 40 × 1.5 mm square pieces using electric discharge wire cutting machine in preparation for arc welding.

Before welding, the samples were cleaned with acetone and ethanol to remove grease and other impurities from the surface of the BMs. The optimized welding parameters were set as follows: voltage at 65 V, current at 12.5 A, and welding speed at 2 mm/s. These parameters ensured full penetration with no significant defects. During welding, both the top and bottom surfaces of the workpiece were protected with 99.99 % pure argon gas to prevent oxidation of the FZ and the HAZ. After welding, samples for microstructural and mechanical performance analysis were obtained using electrical discharge machining.

2.2. Materials characterization

After welding, the sample cross-sections were prepared using conventional metallographic methods, starting with polishing using 600-grit sandpaper and finishing with 3 μm diamond paste. The samples were then etched with Keller's reagent (5 g $CuCl_2$, 5 g HCL and 100 ml C_2H_5OH) to reveal the microstructural features. Optical microscopy (OM) was performed using a Leica DMI5000 M inverted microscope. A scanning electron microscope (SEM) equipped with energy dispersive spectroscopy (EDS), and electron backscatter diffraction (EBSD) analyses were carried out on a JEOL JEM-2100F and a Philips FEG-XL30S, respectively. For the EDS analysis on the JEOL JEM-2100F, the detector used was X-MaxN with Aztec Energy, operating at a voltage of 15 kV with a working distance of 10 mm. For EBSD analysis on the Philips FEG-

XL30S, the voltage is set to 20 kV with a working distance of 12 mm, and a step size of 3 μm is used for overall mapping. The raw EBSD data were processed using TSL OIM Analysis 7.0 software to obtain grain size, texture patterns, and Kernel Average Misorientation (KAM) maps. KAM maps display the local orientation deviation within the microstructure by measuring point-to-point misorientation, which can be used to evaluate the relationship between plastic deformation and microstructural orientation deviations. Typically, high KAM values are associated with regions of high dislocation density or localized strain concentration. To further investigate the microstructural changes in the welded joints, synchrotron X-ray diffraction was employed to scan the entire weld joint. This analysis was conducted at the P07 beamline of PETRA III/DESY using a transmission mode, with an energy of 87.1 KeV (corresponding to a wavelength of 0.14235 Å). In this study, the samples used for synchrotron X-ray experiments were 2 mm thick, corresponding to the thickness of the welded joint. The strong penetration capability of high-energy synchrotron X-rays made this thickness sufficient to meet the experimental requirements, eliminating the need for further thinning and effectively avoiding the introduction of additional strain during sample preparation. The sample preparation process involved lightly polishing the surface oxide layer with 400-grit sandpaper, followed by cleaning with alcohol. Since synchrotron X-ray diffraction is a non-destructive testing technique, a single sample was adequate for the entire experiment. To ensure high-quality diffraction data acquisition, the beam spot size was adjusted before scanning, considering the sample's grain size and the quality of the preliminary Debye-Scherrer rings. During the scan, the beam size was 200 × 200 μm, with a 200 μm step between consecutively analyzed spots. The welded joints were scanned from the HEA BM to the FZ, finishing on the other opposite BM. Hence, by utilizing the defined beam size, step size, along with the known total scan length and scanning path, the precise location of each measurement point within the sample can be accurately identified. A PerkinElmer 2D detector was used to capture the diffraction data. Standard LaB_6 powder was used for the calibration of instrumental parameters using Fit2D software. The sample-to-detector distance was approximately 1440 mm. The sample orientation relative to the laboratory direction was used as a reference, where an azimuthal angle of 0° indicated parallel to the weld direction and 90° indicated perpendicular to the weld direction (the schematic as shown in Fig. 1).

To predict the solidification path of the FZ during non-equilibrium solidification, ThermoCalc was used for thermodynamic calculations. First, an EDS line scan of the FZ was performed to obtain composition data, which served as input data. Next, a custom-developed Python program, combined with the Scheil-Gulliver model, was used to determine the number of phases formed in the FZ during non-equilibrium solidification and the corresponding solidification temperature ranges.

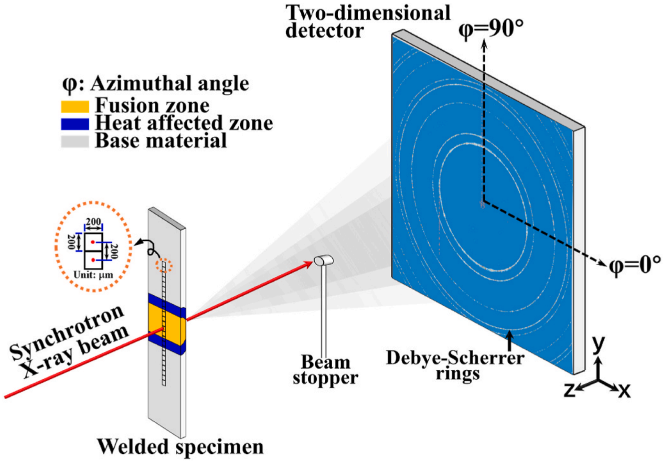

Fig. 1. Schematic of synchrotron X-ray diffraction setup (not to scale).

This approach allowed for the simulation of the impact of welding on the microstructural characteristics of the molten pool. The TCHEA5.1 database was used.

To assess the local mechanical properties, microhardness mapping was performed using a Mitutoyo HM-112 microhardness tester with a load of 500 g and a dwell time of 10 s. The distance between adjacent indentations was set to 200 μm, both longitudinally and transversely. Tensile testing was conducted on an Autograph Shimadzu AG50kNG machine, equipped with a 50 kN load cell, at a displacement rate of 0.001 mm/s. And the loading direction was perpendicular to the weld direction. Additionally, the samples used for tensile tests were dog-bone shaped, with specific dimensions as follows: a gauge length of 25 mm, a width of 1.5 mm, and a thickness of 2 mm. To ensure the reliability and repeatability of the tensile test results, three repeated tensile tests on each sample. Finally, fracture surfaces were analyzed using a Hitachi SU8000 SEM.

3. Results and discussions

3.1. *Microstructure evolution*

Fig. 2 presents the optical microstructure of the dissimilar welded joint between CoCrFeMnNi HEA and 316 stainless steel. This includes the overall cross-sectional macrostructure of the joint (as shown in Fig. 2a) and detailed magnified microstructure images of typical regions such as the BM, HAZ, and FZ, as shown in Fig. 2b), c), d), and e).

From a macroscopic standpoint, the welded joint exhibited full penetration with no visible defects or cracks, demonstrating excellent metallurgical compatibility between the annealed CoCrFeMnNi and 316 stainless steel. Further microstructural analysis reveals that both the BMs and their adjacent HAZ display an equiaxed grain structure with similar grain sizes, rendering the boundary between them nearly indistinguishable. This similarity is attributed to the annealing process that both BMs underwent prior to welding, which homogenized the microstructure and grain size. However, a distinct boundary is evident between the HAZ and the FZ, as indicated by the black dashed lines in Fig. 2d) and e). The FZ, being directly influenced by the heat source, experienced complete melting followed by rapid solidification under non-equilibrium conditions, resulting in a significant modification of the original microstructure. The fine dendritic structures observed within the FZ are governed by the ratio of the temperature gradient (G) to the solidification rate (R) during the solidification process.

To further investigate the microstructural characteristics of the entire welded joint, Fig. 3 provides EBSD characterization data, which include critical information on grain size, texture patterns, and KAM maps. Here, high-angle grain boundaries (HAGB, ranging from 15^o to 62.7°) are utilized to delineate the boundaries between grains. From a macroscopic perspective, Fig. 3a) reveals significant microstructural differences between the FZ and the surrounding regions of the joint. The FZ is marked by the presence of large grains ($d \approx 212.2$ μm), a feature directly related to the weld thermal cycle. These grains initially nucleate from the two cold substrates and, as the molten pool cools, they grow competitively along the direction of the maximum thermal gradient (i.e., towards the weld centerline). For 316 stainless steel and CoCrFeMnNi HEA, grains generally exhibit preferential growth along the (100) direction. However, in the dissimilar welded joints, this typical preferential orientation is disrupted. As shown in Fig. 3d), there is no distinct (100) grain orientation observed. The BMs do no exhibit significant preferential orientation due to the annealing treatment prior to welding. For the FZ, this disruption of (100) orientation observed in the middle of FZ could be driven by the complex temperature gradients within the FZ, the molten pool size effect, and the uncontrolled mixing of the two BMs [1]. These factors contribute to abnormal grain growth and the emergence of new grain orientations that are more favourable than the (100) direction, thereby altering the grain alignment in the solidified FZ. While grains typically tend to grow toward the (100) orientation, in this

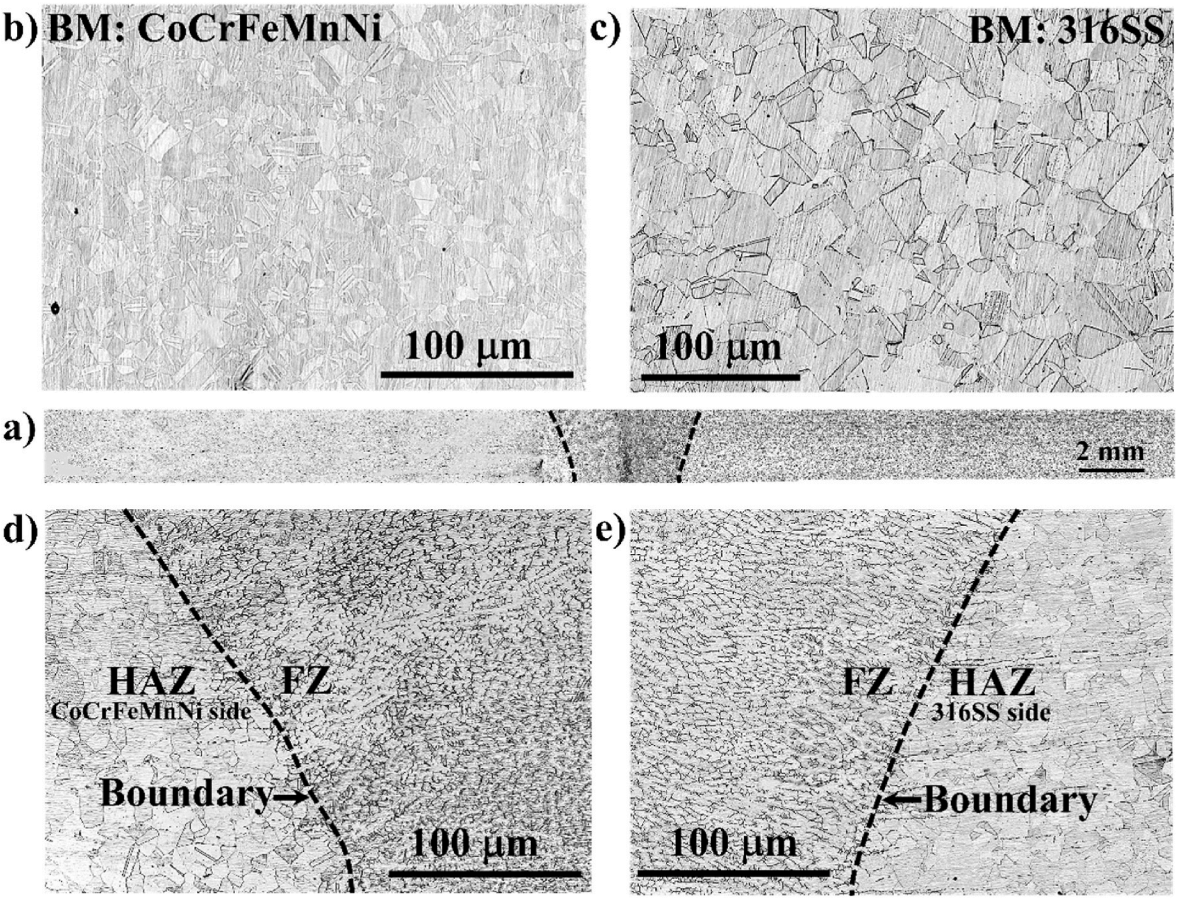

Fig. 2. a) a cross-sectional view of dissimilar GTA-welded CoCrFeMnNi HEA to 316 stainless steel; b)-e) are close-up views of optical/electron microscopy for the CoCrFeMnNi HEA BM, 316 stainless BM, the boundary of HAZ/FZ near the CoCrFeMnNi HEA side and HAZ near the 316 stainless steel, respectively.

case, the unique weld thermal cycle and mixing conditions in the FZ may have suppressed this tendency.

When examining the BMs and their respective HAZs on both sides of the welded joint, it is observed that the initial grain sizes in 316 stainless steel and CoCrFeMnNi HEA are ≈19 μm and ≈14.8 μm, respectively. Upon entering the HAZs (Fig. 3b), the grains in these regions do not exhibit significant growth compared to those in the BMLs (316 stainless steel side: » 19 mm (BM) vs. » 21.3 mm (HAZ); CoCrFeMnNi HEA side: » 14.8 mm (BM) vs. » 15.5 mm (HAZ)), despite these regions are affected by the weld thermal cycle. This minor grain growth trend is primarily attributed to the pre-welding annealing of the BMs, which effectively limited the tendency for grain coarsening in the HAZs. Additionally, the grains in these regions exhibit relatively random orientation with no marked texture (Fig. 3d).

The KAM maps generated from EBSD data processing (Fig. 3c) illustrate the distribution of local misorientations, with lower misorientations represented in blue and the higher in red. Overall, the variation in local misorientation across different regions of the welded joint is not significant, indicating that residual stress/strain in the welded joint is minimal. The average KAM values for the BMs, 316 stainless steel and CoCrFeMnNi HEA, are approximately ≈0.90° and ≈0.78°, respectively. This suggests that the annealing treatment applied to these materials prior to welding has effectively relieved most of the internal stress and strain that may have accumulated during thermomechanical processing of the raw materials. Upon entering the HAZ, the local misorientation does not significantly increase due to the thermal stress induced by the weld thermal cycle, remaining nearly unchanged (316 stainless steel: ≈0.95°; CoCrFeMnNi HEA: ≈0.88°), hinting to the material's strong resistance to thermal stresses.

The energy dispersive spectroscopy (EDS) map presented in Fig. 4 is crucial for understanding the element distribution across the joint. The map indicates that, within the dissimilar joint between CoCrFeMnNi and 316 stainless steel, the element distribution is relatively uniform with no significant macro-segregation.

To investigate the effect of weld thermal cycle on the microstructure across the welded joint, high-energy synchrotron radiation was used to scan the processed materials, from the BM, through the HAZ and FZ, and extending to the BM on the other side. Fig. 5a) depicts the superimposed synchrotron diffraction patterns obtained. Based on changes in intensity, the extent of the FZ is marked by the black dashed line. However, the diffracted intensity in the BM and HAZ on both sides is nearly identical, making it challenging to distinguish the boundaries between these regions. Detailed information on how to differentiate between BM and HAZ will be discussed based on Fig. 6. It is worth noting here that although the X-ray attenuation coefficients of the two materials (316 stainless steel and CoCrFeMnNi HEA) are slightly different ($\mu_{316\ \mathrm{stainless\ steel}} = 0.0096\ \mathrm{cm}^{-1}$ vs. $\mu_{\mathrm{CoCrFeMnNi}} = 0.0093\ \mathrm{cm}^{-1}$), their transmittance under high-energy X-ray (87.1 keV) scanning is remarkably similar ($T_{316\ \mathrm{stainless\ steel}} = 98.2\ \%$ vs. $T_{\mathrm{CoCrFeMnNi}} = 98.1\ \%$). This indicates that the effect of absorption on the diffraction intensity of the two materials is negligible. Therefore, it can be inferred that the observed diffraction peak intensities in the experiment primarily reflect the intrinsic crystal structure characteristics of the materials, rather than being influenced by absorption effects.

Based on phase identification and Rietveld refinement results, the BM of the 316 stainless steel primarily consists of γ-FCC (≈96 %) and δ-BCC (≈2.5 %) phases. This phase identification aligns with previous studies of 316 stainless steel thermo-mechanically processed in the same condition [37]. Additionally, ≈1.5 % of σ phase was detected. The intermetallic σ phase in 316 stainless steel has been a subject of interest.

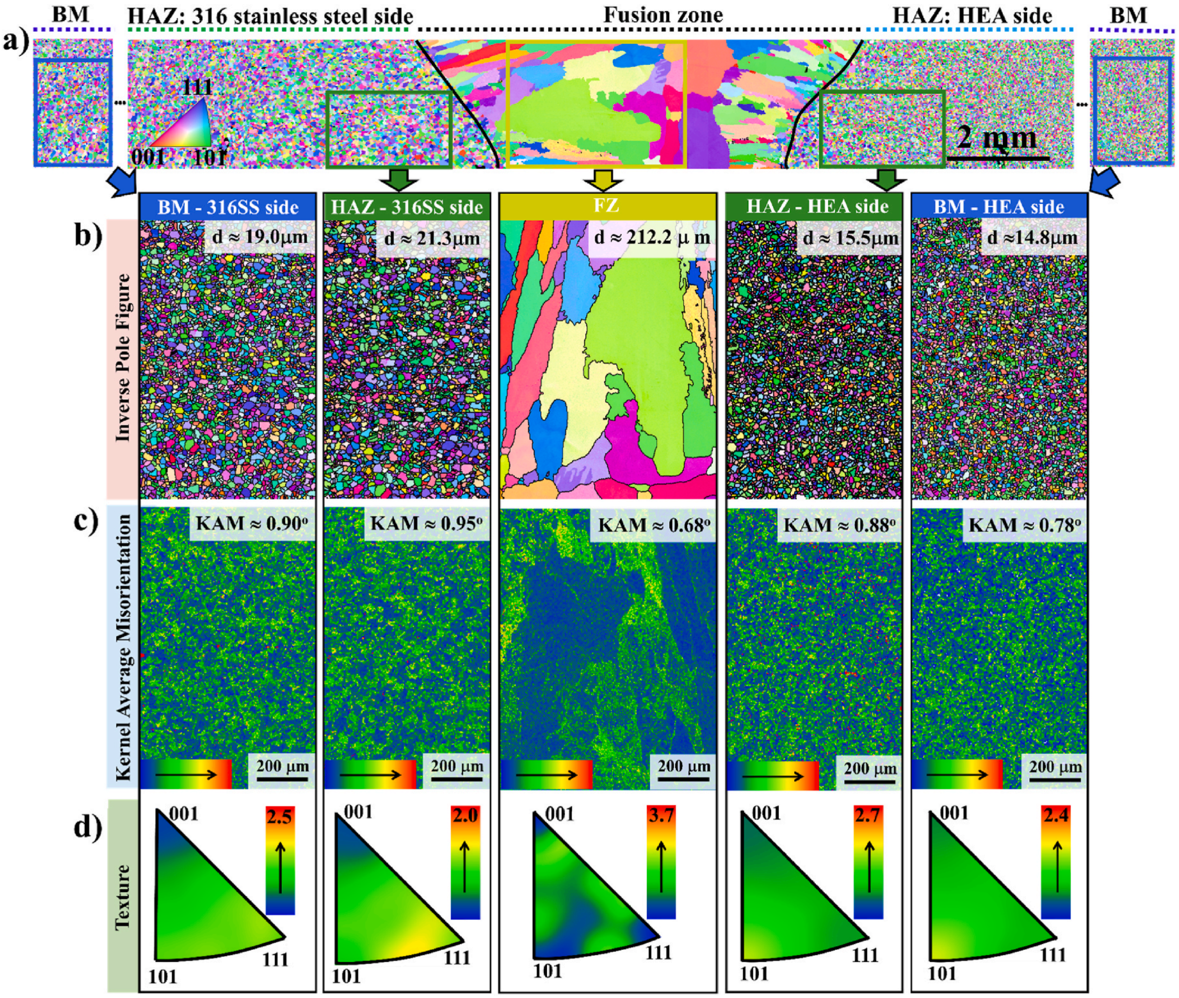

Fig. 3. Microstructure of dissimilar GTA-welded CoCrFeMnNi HEA to 316 stainless steel: a) EBSD maps of the cross-sectionals of the joint; b) -d) are IPF maps, KAM and texture evolution of the BM and HAZ in the 316 stainless steel side, FZ, HAZ in the CoCrFeMnNi HEA side and CoCrFeMnNi BM (from left to right).

According to existing literature [42], the formation of σ phase is influenced by various factors, including chemical composition, annealing conditions, and thermo-mechanical processing conditions. Notably, the Cr and Mo present in 316 stainless steel can aid in the rapid precipitation of σ, especially under high-temperature heat treatment [43–45]. Moreover, the presence of δ-BCC phase has been confirmed to accelerate the precipitation kinetics [46,47]. Considering that the 316 stainless steel BM in this study underwent hot rolling, cold rolling, and annealing prior to welding, the presence of σ phase is therefore justified. Then, in the HAZ near the 316 stainless steel, no new phases beyond those reported in the BM were observed. However, a solid-state phase transformation was detected: δ-BCC → σ phase. The volume fraction of σ phase increased from ≈1.5 % to ≈2.3 %, while the δ-BCC phase decreased from about ≈2.5 % to ≈1.7 %. It has been reported [48] that specific heat treatment conditions can induce the phase transformation of δ-BCC to σ phase in 316 stainless steels. Therefore, it can be inferred that the weld thermal cycle in the HAZ is akin to high-temperature annealing, resulting in the dissolution of the δ-BCC phase and its transformation into the σ phase. Turning to the other side of the joint, which includes the CoCrFeMnNi BM and the adjacent HAZ, the phase structure is predominantly composed of an FCC matrix phase (≈98.6 %), along with a small amount of ≈1.4 % Cr–Mn oxide. This occurrence has been consistently reported in previous studies and is attributed to material contamination during the high-temperature processing of the raw materials [49]. Specifically, Cr and Mn elements have a strong affinity with oxygen, making them highly susceptible to oxidation under such conditions, leading to the formation of Cr-Mn-based oxides. This phenomenon has been confirmed in previous studies, such as the investigation of the high-temperature oxidation behaviours of CoCrFeMnNi HEAs by Kim et al. [50]. In the HAZ, no new phase structures were detected. However, the Cr-Mn oxide content increased slightly to about ≈2.1 %, which is also attributed to the high affinity of Cr and Mn elements for oxygen at elevated temperatures aiding the formation of Cr-Mn-based oxides. Although Cr-Mn oxides are indeed present in the welded joint, their presence does not cause any phase changes or microstructural alterations. In other words, Cr-Mn oxides primarily function as impurities in the overall microstructure of CoCrFeMnNi HEA and HAZ, with almost no impact on the overall microstructure.

Finally, in the FZ where the two BMs have completely melted and mixed, FCC phase, ≈4.9 % BCC phase, and about ≈2.3 % Cr–Mn oxides were detected. The presence of Cr-Mn oxide has been confirmed by the line scan results from DES (see Fig. 5c). The appearance of the BCC phase is attributed to the ample Fe supplied by the 316 stainless steel base material during melting. Compared to the 316 stainless steel BM and the HAZ, the BCC phase content in the FZ has significantly increased to about ≈4.9 %. It is noteworthy that the standard CIF files used in the MAUD software are sourced from the Crystallography Open Database. Through retrieval, the identified phase structures - FCC, BCC, σ phase, and Cr-Mn oxide - correspond to the following Crystallography Open Database (COD) IDs: 1534888, 1100108, 9016031, and 5910036, respectively.

To distinguish the boundary between the BM and the HAZ, Fig. 6

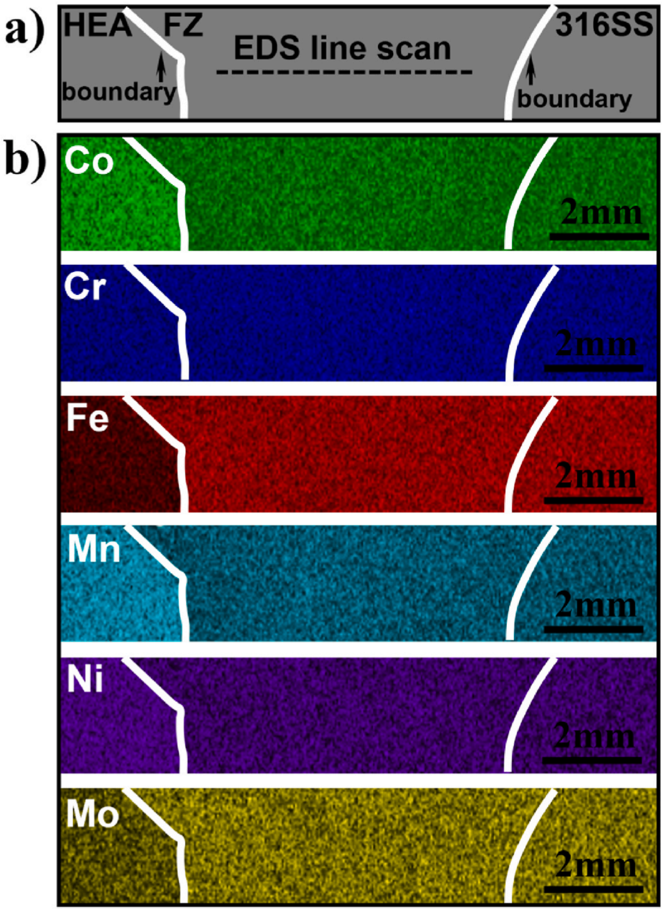

Fig. 4. EDS mapping of GTA-welded CoCrFeMnNi HEA to 316 stainless steel.

shows the evolution of the intensity (Fig. 6a), FWHM (Fig. 6b), and d-spacing (Fig. 6c) of the (311) diffraction peak along the welding direction (azimuthal angle integration around 0°) and perpendicular to the welding direction (azimuthal angle integration around 90°). Here, the (311) diffraction peak (refer to Fig. 5a and b) was selected for analysis due to its low sensitivity to intergranular strain [2]. First, changes in diffracted intensity (Fig. 6a) are examined. In the BM and HAZ, the diffraction intensity of the (311) plane exhibits only minor fluctuations in both directions, attributed to the similarity in grain size and texture between these regions (Fig. 3b and d). However, upon entering the FZ, grain coarsening (refer to Fig. 3a) increases the likelihood of regions with consistent or similar grain orientations forming within the probed area. This enhances the diffraction effect, leading to a significant increase in diffracted intensity. Although this characteristic indicates the presence of the FZ, it is insufficient for clearly distinguishing the BM from the HAZ. Thus, while the intensity evolution reflects the existence of the FZ, it cannot effectively differentiate between the BM and the HAZ. Next, the changes in Full Width at Half Maximum (FWHM) (Fig. 6b) are analyzed. The broadening of FWHM results from a combination of internal strain and grain size variation, with the internal strain arising from the accumulation of structural defects such as dislocations and stacking faults. Given the similarity in KAM values (Fig. 3c) and grain size (Fig. 3b) between the BM and HAZ, the similarity in FWHM between these two regions is expected. Therefore, the changes in FWHM also fail to effectively distinguish these regions.

The most striking microstructure observation is the significant variation in d-spacing (Fig. 6c). In the BM region, where external forces and the high temperatures from the weld thermal cycle are absent, the d-spacing remains stable in both principal directions. However, this stability is disrupted upon entering the HAZ. Perpendicular to the weld (azimuthal angle of 90°), the increased thermal motion of atoms induced by the weld thermal cycle causes a substantial increase in lattice spacing, which gradually decreases as the heat dissipates away from the weld. In contrast, parallel to the weld (azimuthal angle of 0°), tensile or compressive stresses during weld formation and cooling lead to fluctuations in lattice spacing, resulting in both notorious changes. In the FZ of the weld, the d-spacing undergoes significant changes. The increase in d-spacing reflects the expansion of the lattice due to thermal expansion or tensile stresses, and during cooling, as the stress is gradually released, the d-spacing may stabilize or slightly contracts. Besides, the welding process often involves the mixing and redistribution of elements, which can lead to variations in the local composition within the FZ. These compositional changes can affect the lattice parameters and, consequently, the d-spacing, further contributing to the complex microstructural evolution observed in welded joints. Thus, these changes reveal the effect of weld thermal cycling on the lattice structure, reflecting the action of thermal stresses, temperature changes and composition redistribution on the internal lattice of the material during the welding process. This distinct pattern of d-spacing evolution clearly delineates the boundaries between the BM, HAZ, and FZ, highlighting the complementarity between synchrotron X-ray diffraction and electron microscopy to clearly delineate each region of the welded joint.

It is important to clarify that while the weld thermal cycle can alter the local d-spacing and introduce lattice strain, this does not necessarily lead to the direct generation of a significant number of defects, such as dislocations, which would impact the FWHM. The formation of dislocations is a complex process influenced by several factors, including temperature gradients, cooling rates, and the material's intrinsic plastic deformation capacity. Therefore, even with changes in lattice spacing, the FWHM may not always exhibit a significant corresponding variation.

3.2. *Thermodynamic calculations*

To understand the phase structure that developed within the FZ, the non-equilibrium solidification thermodynamic model (Scheil-Gulliver) based on CalPhaD was used to predict the solidification temperatures and the potential number of phases formed (Fig. 7a). Input data were derived from a series of EDS point scans performed along the black dashed line shown in Fig. 4a). Detailed EDS measurements of the composition are provided in supplementary materials. These thermodynamic calculations indicate that the solidification temperatures at different locations within the FZ range between 25 and 80 °C, stemming from the non-homogeneous dilution/mixing ratios at various points within the FZ. Despite these variations in solidification temperatures, the predicted number of phase structures consistently remains two: FCC and BCC phases.

To further reproduce the non-equilibrium solidification behavior of the FZ, including the solidification path and precipitated phases, the average composition obtained from the EDS area mapping of the FZ was used as input in the Scheil-Gulliver model, and the results are presented in Fig. 7b). As can be seen from the figure, during the non-equilibrium solidification process, the FCC matrix phase forms first, followed by the joint formation of FCC and BCC phases in the remaining liquid. The entire solidification process is completed at approximately ≈1392 °C. Compared to the phase identification results in the FZ obtained from synchrotron radiation (Fig. 5b), the thermodynamic model did not predict the presence of Cr-Mn oxides, since no oxygen data was used as input. To address limitations in Cr-Mn oxide predictions and oxidation processes, two approaches were attempted. First, using TCHEA and TCOX databases together encountered conflicts due to TCHEA's lack of oxygen data. Second, although TC-PRISMA was applied for oxide precipitation, Cr-Mn oxides remain absent in HEA databases, and the observed oxides primarily result from processing contamination, which cannot be fully replicated thermodynamically. This indicates that the current databases have certain limitations in handling systems containing oxides. Nevertheless, since we know the oxide fraction prior

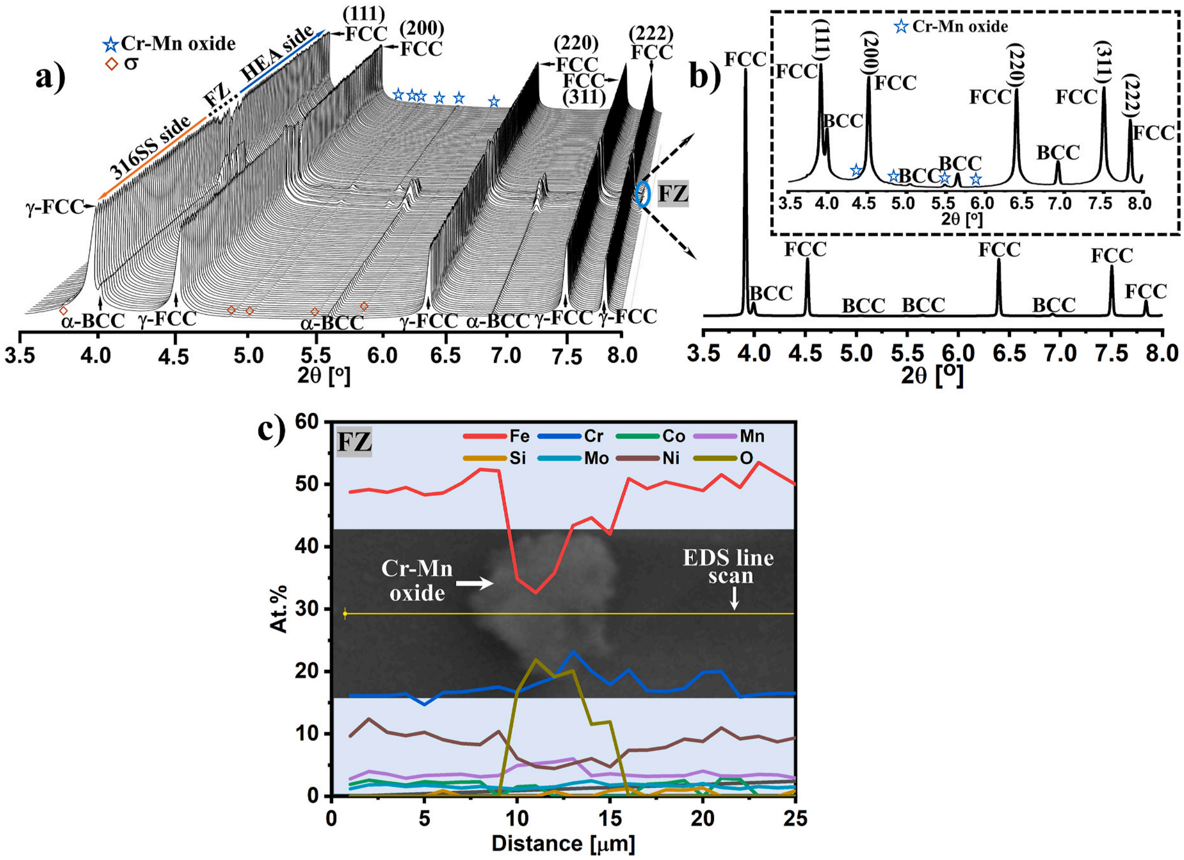

Fig. 5. a) 3D plot of GTA-welded CoCrFeMnNi HEA to 316 stainless steel using synchrotron X-ray diffraction; b) representative diffraction pattern from FZ; c) EDS line scans along the yellow line. (For interpretation of the references to colour in this figure legend, the reader is referred to the Web version of this article.)

(≈1.4 %) and after welding in the HAZ and FZ (≈2.1 and ≈ 2.3 %), we can assess how the weld thermal cycle contributes to oxidation at each location of the joint. It should be noticed that the change in oxide fraction is relatively low since inert shielding gas was used to protect the thermally affected regions during the high temperature processing employed in this work.

Fig. 7c) and d) illustrate the solidification paths of the two BMs, 316 stainless steel and CoCrFeMnNi HEA. The phase structures predicted by thermodynamic calculations using the Scheil model are in excellent agreement with the actual phases observed through synchrotron X-ray diffraction measurements for both BMs (Fig. 5a). For 316 stainless steel, the Scheil model predicts the formation of both γ-FCC and α-BCC phases, while for CoCrFeMnNi HEA, only the FCC phase is predicted.

3.3. *Mechanical response*

Building on the previously revealed microstructural evolution, the next focus is to evaluate the impact of the weld thermal cycle on the local mechanical properties of the weld, which is crucial for assessing its potential use as a structural component.

Fig. 8 illustrates the microhardness distribution of the welded joint. The hardness values of the 316 stainless and CoCrFeMnNi HEA BMs are ≈165 and ≈180 HV0.5, respectively, indicating relatively low hardness in their annealed state. In the HAZ, the hardness distribution on both sides remains similar to that of the corresponding BMs. This similarity is attributed to the comparable grain size and dislocation density between the HAZ and the BM. However, there is a slight increase in hardness in FZ, reaching ≈195 HV0.5. Considering the mixing of the two BMs and the nearly negligible segregation phenomenon, this characteristic facilitates the development of solid solution strengthening effects. This effect primarily arises from lattice distortion caused by atomic mismatch. Notably, elements such as Mo, which have relatively large atomic radii and are present in the 316 stainless steel BM, are typical solid solution strengthening agents [51]. Therefore, it can be reasonably inferred that when Mo is introduced into the melt pool, it becomes the predominant factor driving the enhancement of solid solution strengthening in the FZ. Furthermore, the increase in hardness within the FZ can also be attributed to trace amounts of carbon introduced from both BMs. Previous studies by Li [52] have shown that adding small quantities of carbon to CoCrFeMnNi HEAs can significantly enhance the material's strength. However, due to the very low carbon content in both the 316 stainless steel and the CoCrFeMnNi alloy, the strength enhancement is relatively limited. Similarly, while hard phases, such as the BCC phase, are present in the FZ, previous research indicates [53] that their extremely low content does not significantly impact hardness. Based on the above discussion, it can be concluded that the primary factor contributing to the hardness enhancement in the FZ of this dissimilar welded join is the solid solution strengthening effect. This microhardness gradient demonstrates the varying mechanical behaviour caused by the development of different microstructures formed due to the thermal cycle associated to the welding process.

To further investigate the microstructural evolution mechanisms and their impact on the hardness distribution, this study analyzes the evolution of FWHM across the joint. In both the BMs and HAZ, FWHM shows similarities (refer to Fig. 6b), reflecting the consistency in grain size and dislocation density between these regions, which aligns with the hardness distribution observed on both sides. In contrast, in FZ, FWHM significantly increases, primarily due to grain coarsening. Analysis of the KAM values indicates that internal strains in the FZ did not significantly increase, so the change in FWHM is mainly attributed to changes in grain size. According to the Hall-Petch relationship, an increase in grain size leads to a decrease in hardness, which is consistent

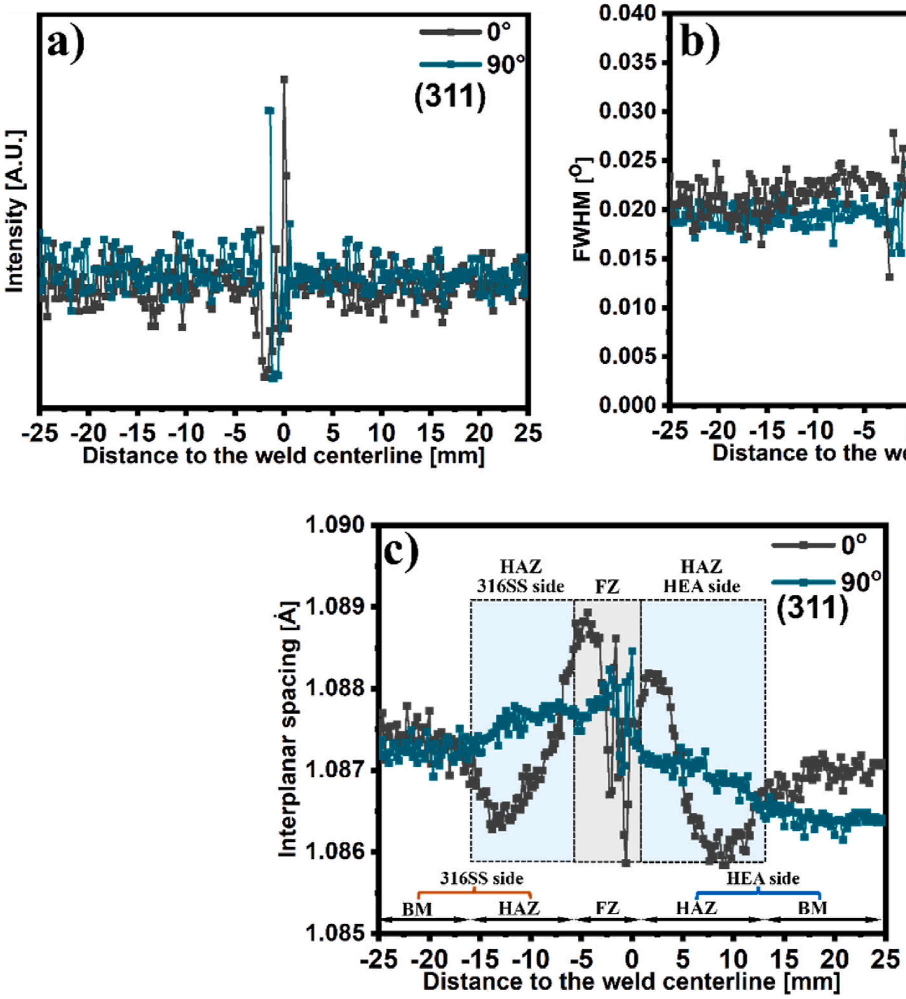

Fig. 6. Evolution of a) Intensity; b) Full Width at Half Maximum (FWHM); and c) Interplanar spacing for GTA-welded CoCrFeMnNi to 316 stainless steel along the 0 and 90^{o} azimuthal angles.

with the hardness data showing the lowest hardness in the FZ. In conclusion, the evolution of FWHM not only reveals microstructural changes but also effectively correlates with the hardness distribution: when FWHM remains stable, grain size and dislocation density are consistent, and the hardness distribution remains unchanged; when FWHM increases, grain size increases, and hardness tends to decrease. By combining hardness testing with FWHM analysis, this study clarifies the dual impact of the weld thermal cycle on both microstructure and mechanical properties.

A representative stress-strain curve of the dissimilar welded joint between CoCrFeMnNi and 316 stainless steel is presented in Fig. 9. Further analysis revealed that the ultimate tensile strength of the welded joint lies between that of the two BMs, while the elongation at fracture is lower. The reasons for the mechanical properties of welded joints being worse than those of their BMs can be attributed to the combined effect of: 1) Microstructural inhomogeneity: the weld thermal cycle leads the development of an overall microstructural heterogeneity in the joint, which can adversely affect the overall performance of the joint; 2) σ phase precipitation in the HAZ of 316 stainless steel: at this HAZ, part of the δ-BCC phase transforms into the σ phase under the effect of weld thermal cycle. As a brittle and hard phase, σ phase tends to cause stress concentration during tensile deformation, significantly reducing the elongation at fracture and negatively impacting the tensile performance of the joint; 3) Hardness differences: there is a significant hardness disparity between the FZ and the HAZ, and this difference can lead to stress concentration during tensile loading, particularly at the soft-hard boundary, accelerating fracture. Although the ultimate strength and ductility of this joint are reduced compared to the respective BMs [37], its distinct mechanical properties (ultimate strength: ≈450 MPa; ductility: ≈6.2 %) still indicate potential for structural applications. Here, it is important to emphasize that the three factors discussed above, which affect mechanical properties, are based on results from two-dimensional characterization. However, we do not exclude the possibility of small-scale defects, such as micro-porosities or sub-surface voids, which cannot be detected using the two-dimensional characterization methods employed in this study. To further improve the evaluation of these potential defects, future studies will include supplementary analysis using advanced techniques such as X-ray Computed Tomography (XCT).

Observation of the macroscopic fracture surface revealed that the failure of the dissimilar welded joint occurred in the HAZ on the 316 stainless steel side, adjacent to the FZ. Based on previous microstructural and hardness analyses, the fracture can be attributed to two main factors: the relatively low hardness in this region and the stress concentration effect caused by the presence of σ phase. Specifically, during tensile deformation, the BM on the 316 stainless steel side and its HAZ are the regions with comparatively lower hardness within the joint, leading them to bear more load initially. Notably, the σ phase content in the HAZ is also higher than in the 316 stainless steel BM (≈2.3 % vs. ≈1.5 %, as shown in Fig. 5). As a hard and brittle phase, σ phase easily becomes a focal point for stress concentration during tensile deformation, thereby accelerating fracture. Furthermore, although the content of

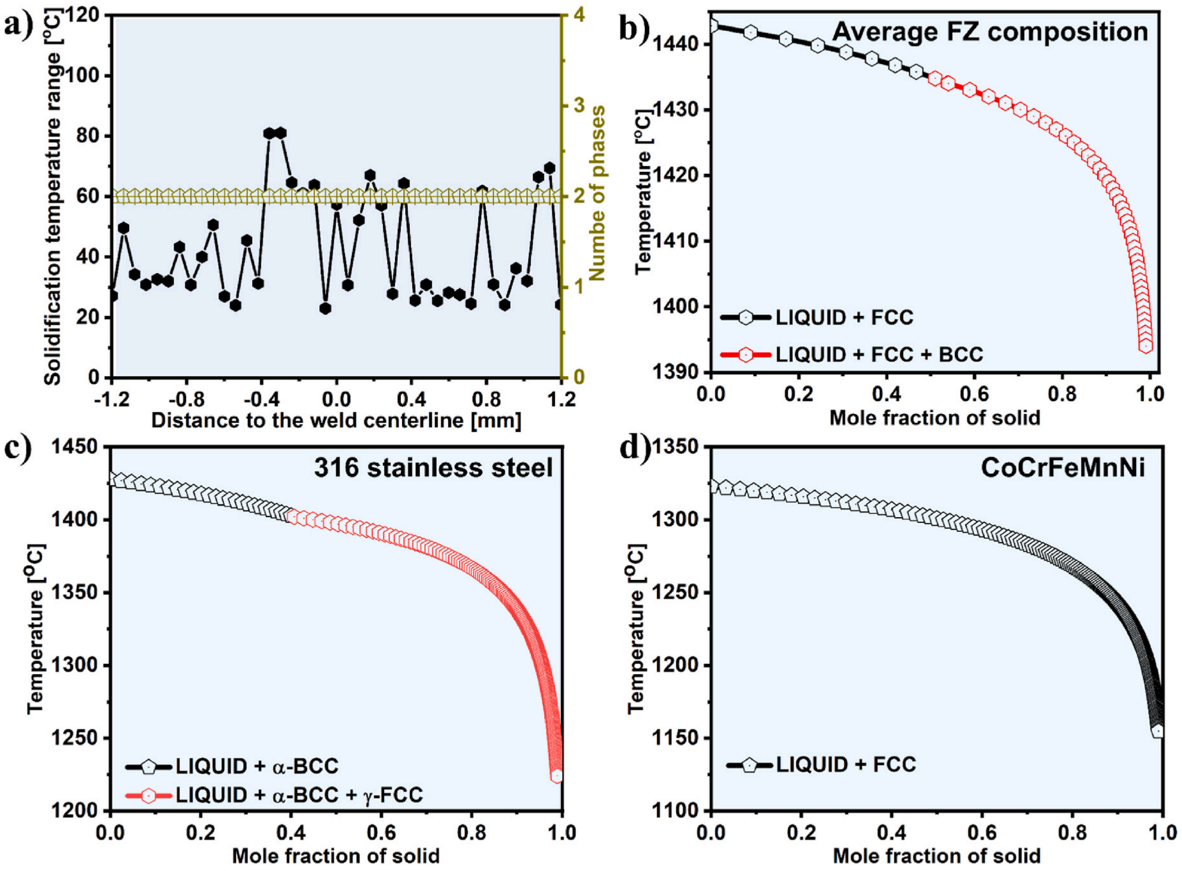

Fig. 7. a): CalPhaD-predicted solidification temperature range and number of phases using the EDS measured composition along the black dashed line as shown in Fig. 3 a); b): Simulation of non-equilibrium solidification path using Scheil-Gulliver model with the average composition measured by the EDS area mapping as input; c): Scheil calculations for 316 stainless steel base material; d): Scheil calculations for CoCrFeMnNi base material.

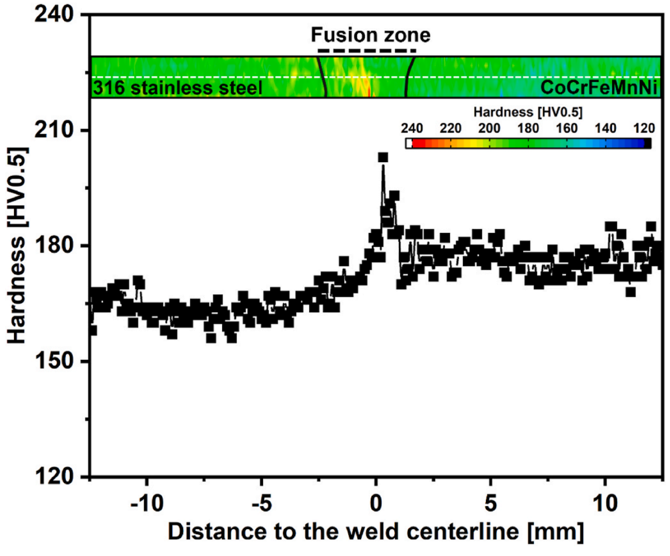

Fig. 8. Microhardness mapping of dissimilar GTA-welded CoCrFeMnNi HEA to 316 stainless steel, and representative line scan along the mid-hight of the joint.

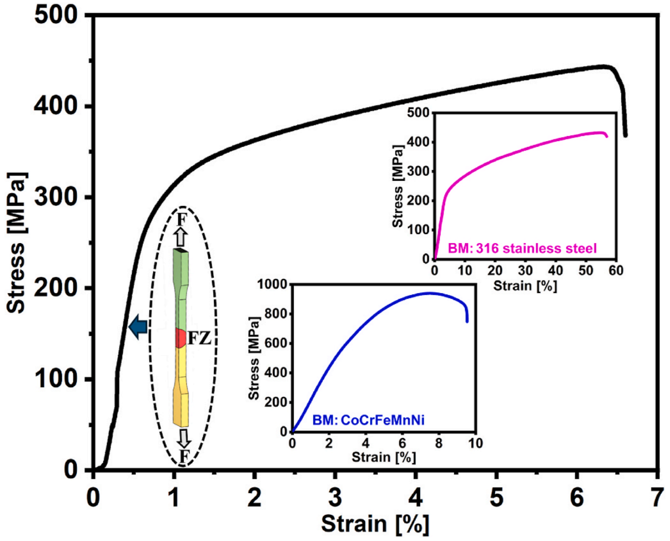

Fig. 9. Tensile strain-stress curve of dissimilar GTA-welded joint of CoCrFeMnNi HEA to 316 stainless steel. The inserts detail the representative stress/strain curves of the 316 stainless steel (blue colour) and CoCrFeMnNi high entropy alloy (red colour) BMs. (For interpretation of the references to colour in this figure legend, the reader is referred to the Web version of this article.)

Cr-Mn oxide particles in the fracture region is higher compared to the BM, existing research [3] suggests that these oxide particles do not significantly impact mechanical properties. Therefore, the hypothesis that oxide particles are the primary cause of the fracture can be ruled out.

Thus, the fracture of the dissimilar welded joint between CoCrFeMnNi and 316 stainless steel is attributable to the combined effects of low hardness in the HAZ on the 316 stainless steel side and stress concentration induced by the σ phase. To improve the mechanical properties and fracture resistance of the joint, future research will concentrate on optimizing the welding process to minimize the formation of the σ phase and on exploring strategies to enhance the hardness of the HAZ.

To further investigate the mechanism of tensile fracture failure, EBSD analysis was performed on one end of the fractured specimen, focusing specifically on the regions marked as A, B, C, and D, as shown in Fig. 10a). The analysis revealed that the grain size in the BM region of the fractured specimen is ≈ 18.5 μm, confirming that the analyzed specimen originates from the 316 stainless steel side. Notably, the grain size near the fracture site increases to about ≈23.2 μm, with a pronounced elongated morphology. Compared to the size and morphology of the equiaxed grains before tensile testing (as shown in Fig. 3), this change indicates that grains underwent intense plastic deformation during the tensile process, elongating along the tensile direction. This observation directly reflects the high-stress plastic deformation experienced by the material.

Additionally, the KAM data was used to assess the internal micro-strain and defect density of the material. The results indicate that the KAM value reaches its maximum, ≈1.37°, near the fracture site, suggesting a substantial accumulation of micro-strain and defects in this region. Observations of the HAZ at approximately ≈3.6 mm and ≈5.4 mm away from the fracture site reveal that the grain sizes in these areas (≈20.3 μm and ≈21.3 μm, respectively) remain largely consistent with the grain size before tensile testing (≈21.3 μm), and the KAM values are lower compared to those near the fracture site. This indicates that the microstructure in the HAZ further from the fracture site remains relatively stable, unaffected by intense plastic deformation during tension. This confirms that the fracture primarily occurred in the localized regions of the HAZ near the FZ.

In conclusion, the variations in grain size and morphology, along with the increase in KAM values from the BM region to the fracture site, reflect the gradual transition of the material from a stable state to a failure state during the tensile process. The high-stress concentration induced by σ phases as discussed above and accumulated plastic deformation near the fracture surface leads to significant changes in the material's internal microstructure, ultimately causing its fracture.

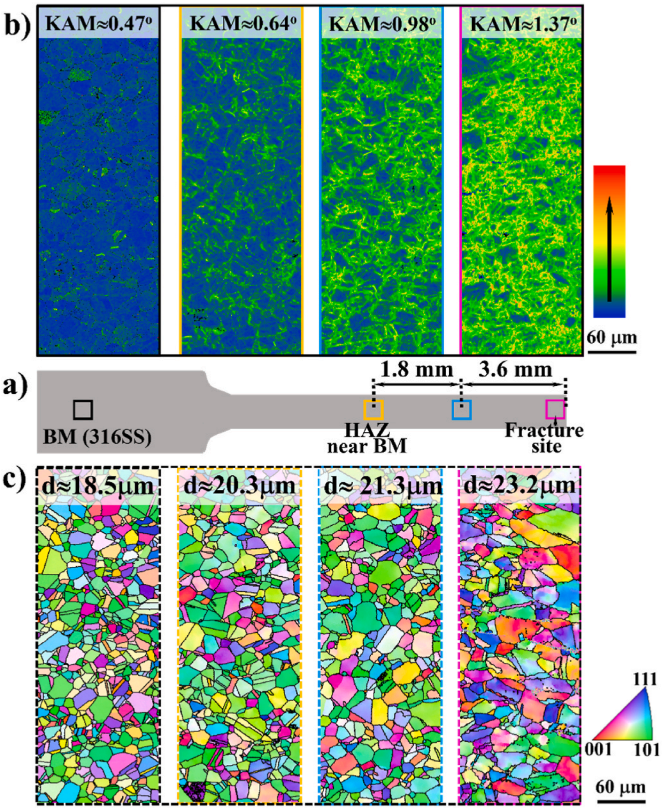

Fig. 10. b) KAM maps and c) IPF maps of the fractured specimen considering different locations across the joint, as marked in a). From left side to right side: BM, HAZ, HAZ and fractured site.

This study systematically investigates, for the first time, the evolution of microstructure and mechanical properties of dissimilar joints between CoCrFeMnNi HEA and 316 stainless steel under GTAW conditions, addressing a gap in the field. Compared to prior studies employing laser welding, three main differences are observed. Firstly, differences in heat input and phase structures: Due to its high energy density and concentrated heat source, laser welding [31,37] results in a narrow HAZ (approximately ≈ 50 μm), effectively suppressing excessive columnar grain growth in the FZ and forming a single FCC phase. In contrast, GTAW-ed, with its higher heat input, leads to a significantly wider HAZ (≈10 mm), with an average columnar grain size in the FZ reaching ≈ 212 μm. Additionally, a solid-state phase transformation from δ-BCC to σ phase was observed on the 316 stainless steel side, while the FZ contained minor amounts of BCC phases and Cr-Mn oxides, which are closely related to the higher heat input. Secondly, differences in mechanical properties: Although the tensile strengths of laser-welded and GTAW-ed joints are comparable (≈450 MPa vs. ≈ 449 MPa), the ductility of the laser-welded joints (≈5 %) is notably lower than that of the GTAW-ed joints (≈6.2 %). This indicates that, by optimizing welding parameters, GTAW-ed joints can achieve mechanical properties similar to those of laser-welded joints. Lastly, significant differences in the location of tensile fracture failure: In the case of laser-welded joints, failure occurs in the FZ, primarily due to the unfavourable microstructure in this region, which consists of large columnar grains. For GTAW joints, failure occurs near the HAZ of the 316 stainless steel, which is mainly attributed to the presence of hard σ phase and the combined effect of microstructural inhomogeneity in that region. It is worth noting that laser welding, with its stringent requirements for heat input control, is more suitable for precision applications, while GTAW, with its lower equipment costs and simpler operation, is better suited for large-scale industrial applications. In conclusion, despite certain advantages of laser welding in specific aspects, its mechanical properties did not demonstrate significant superiority in the connection of CoCrFeMnNi HEA and 316 stainless steel studied here. This also highlights that traditional GTAW methods can achieve high-quality welded joints through parameter optimization.

In conclusion, by comparing the welded joints of CoCrFeMnNi HEAs and 316 stainless steel obtained using these two welding techniques (GTAW and laser welding), it can be concluded that GTAW is often preferred over laser welding. This preference is due to its cost-effectiveness, ease of operation, and better mechanical performance, particularly in terms of ductility. Moreover, GTAW is especially well-suited for large-scale manufacturing, repair operations, and applications where high precision is not critical. Its versatility in handling thicker sections and more complex joint geometries, combined with its lower sensitivity to surface conditions, makes it a practical and reliable choice for many applications.

4. Conclusions

This study systematically examines the effects of the weld thermal cycle on the microstructural evolution and mechanical properties of dissimilar GTA-welded joints of CoCrFeMnNi HEA to 316 stainless steel, combining microstructural characterization with mechanical property testing. The main conclusions are as follows.

- The annealed CoCrFeMnNi HEA and 316 stainless steel BMs exhibit excellent metallurgical bonding during arc-based welding.
- EDS analysis reveals a uniform distribution of elements within the welded joint, with no observed segregation.

- The HAZ on the 316 stainless steel side primarily consisted of δ-BCC and γ-FCC phases, with a phase transformation from δ-BCC to σ phase being observed in the HAZ. On the CoCrFeMnNi side, a slight increase in Cr-Mn oxide content was noted in the HAZ, though this did not adversely affect mechanical properties. The BCC phase detected in the FZ was attributed to the Fe element provided by the 316 stainless steel BM.
- The microstructure, grain size, and hardness distribution across both BMs and their adjacent HAZs are highly similar. This is attributed to the annealing treatment applied before welding, which homogenized the microstructure and grain size, making the boundary between the BM and the HAZ difficult to distinguish.
- The interplanar spacing evolution, as determined by synchrotron X-ray diffraction, can be used to differentiate the various regions of the welded joint.
- The highest average hardness was found in the FZ, resulting from a combination of factors which include BCC precipitates, minor incorporation of carbon introduced with the FZ, as well as solid solution strengthening, but solid solution strengthening is the key factor, primarily due to the solid solution strengthening.
- EBSD analysis of the tensile fractures revealed that the fracture occurred in the HAZ near the FZ on the 316 stainless steel side. The grain size in the fracture region increased, and the grain morphology changed from equiaxed to elongated, mainly due to stress concentration induced by the σ phase and the accumulation of plastic deformation in regions of high-stress concentration.

Overall, this study successfully produced fully penetrated, defect-free welded joints and established the correlation between welding processes, microstructural evolution, and mechanical properties. Future research will focus on further optimizing the welding parameters and explore the potential use of post-weld heat treatments to reduce the σ phase content in the joint, while exploring strategies to increase the hardness of the HAZ to further improve the mechanical properties and fracture toughness of the joints.

CRediT authorship contribution statement

Jiajia Shen: Writing – review & editing, Writing – original draft, Visualization, Validation, Software, Methodology, Investigation, Formal analysis, Data curation, Conceptualization. **Rae Eon Kim:** Methodology, Formal analysis, Data curation. **Jingjing He:** Visualization, Methodology, Investigation, Conceptualization. **J.G. Lopes:** Visualization, Validation, Methodology, Investigation. **Jin Yang:** Visualization, Validation, Investigation, Conceptualization. **Zhi Zeng:** Visualization, Validation, Investigation, Conceptualization. **N. Schell:** Visualization, Validation, Resources, Conceptualization. **Hyoung Seop Kim:** Writing – review & editing, Writing – original draft, Visualization, Validation, Resources, Project administration, Methodology, Conceptualization. **J. P. Oliveira:** Writing – review & editing, Writing – original draft, Visualization, Validation, Supervision, Resources, Project administration, Methodology, Investigation, Funding acquisition, Conceptualization.

Declaration of competing interest

The authors declare that they have no known competing financial interests or personal relationships that could have appeared to influence the work reported in this paper.

Acknowledgements

JS and JPO acknowledge Fundação para a Ciência e a Tecnologia (FCT - MCTES) for its financial support via the project UID/00667/2020 (UNIDEMI). JS and JPO acknowledge the funding by national funds from FCT - Fundação para a Ciência e a Tecnologia, I.P., in the scope of the project's LA/P/0037/2020, UIDP/50025/2020 and UIDB/50025/2020 of the Associate Laboratory Institute of Nanostructures, Nanomodelling and Nanofabrication – i3N. JS acknowledges the China Scholarship Council for funding the Ph.D. grant (CSC NO. 201808320394). This work was supported by the National Research Foundation of Korea (NRF) with a grant funded by the Korea government (MSIP) (NRF-2021R1A2C3006662). The authors acknowledge DESY (Hamburg, Germany), a member of the Helmholtz Association HGF, for the provision of experimental facilities. Beamtime was allocated for proposal I-20210899 EC. The study was supported by the International Cooperation Project of Ningbo City, No. 2023H018. The support is gratefully acknowledged. The research leading to this result has been supported by the project CALIPSOplus under the Grant Agreement 730872 from the EU Framework Programme for Research and Innovation HORIZON 2020. The research was supported by the International Cooperation Project of Ningbo City, No. 2023H018, the support is gratefully acknowledged.

Appendix A. Supplementary data

Supplementary data to this article can be found online at https://doi.org/10.1016/j.msea.2024.147664.

Data availability

Data will be made available on request.

References

[1] Y. Ren, R. Skilton, A review of pipe cutting, welding, and NDE technologies for use in fusion devices, Fusion Eng. Des. 202 (2024) 114396, https://doi.org/10.1016/j.fusengdes.2024.114396.

[2] J. Xin, H. Zhang, W. Sun, W. Wang, D. Wu, B. Lyu, F. Shen, Z. Fang, C. Huang, L. Li, Microstructure evolution of austenitic stainless steels under high-cycle-fatigue loading at deep cryogenic temperature, Scr. Mater. 226 (2023) 115223, https://doi.org/10.1016/j.scriptamat.2022.115223.

[3] Y. Zhong, L.-E. Rännar, L. Liu, A. Koptyug, S. Wikman, J. Olsen, D. Cui, Z. Shen, Additive manufacturing of 316L stainless steel by electron beam melting for nuclear fusion applications, J. Nucl. Mater. 486 (2017) 234–245, https://doi.org/10.1016/j.jnucmat.2016.12.042.

[4] P. Zhang, H. Jian, L. Yin, J. Liu, Z. Cai, Y. Tong, Corrosion resistance and mechanical properties of Cr-Rich 316 stainless steel coatings fabricated by the TIG process using flux-cored wires, Molecules 29 (2024) 1785, https://doi.org/10.3390/molecules29081785.

[5] P. Ebrahimzadeh, L.B. Peral, R. González-Martínez, E. Mardaras, I. Fernández-Pariente, Influence of severe surface plastic deformation induced by shot peening on microstructure and corrosion resistance of fine grained 316 L stainless steel, Corros. Sci. 231 (2024) 111988, https://doi.org/10.1016/j.corsci.2024.111988.

[6] B. Cantor, I.T.H. Chang, P. Knight, A.J.B. Vincent, Microstructural development in equiatomic multicomponent alloys, Mater. Sci. Eng. A 375–377 (2004) 213–218, https://doi.org/10.1016/j.msea.2003.10.257.

[7] J.-W. Yeh, S.-K. Chen, S.-J. Lin, J.-Y. Gan, T.-S. Chin, T.-T. Shun, C.-H. Tsau, S.-Y. Chang, Nanostructured high-entropy alloys with multiple principal elements: novel alloy design concepts and outcomes, Adv. Eng. Mater. 6 (2004) 299–303, https://doi.org/10.1002/adem.200300567.

[8] M. Seifi, D. Li, Z. Yong, P.K. Liaw, J.J. Lewandowski, Fracture toughness and fatigue crack growth behavior of as-cast high-entropy alloys, JOM 67 (2015) 2288–2295, https://doi.org/10.1007/s11837-015-1563-9.

[9] S. Liu, M. Hu, L. Xiao, G. Feng, K. Song, W. Song, J. Qiao, Effects of strain rate and low temperature on dynamic behaviors of additively manufactured CoCrFeMnNi high-entropy alloys, Mater. Sci. Eng. A 913 (2024) 147100, https://doi.org/10.1016/j.msea.2024.147100.

[10] A. Raza, H.J. Ryu, S.H. Hong, Strength enhancement and density reduction by the addition of Al in CrFeMoV based high-entropy alloy fabricated through powder metallurgy, Mater. Des. 157 (2018) 97–104, https://doi.org/10.1016/j.matdes.2018.07.023.

[11] F.C. Garcia Filho, S.N. Monteiro, Welding joints in high entropy alloys: a short-review on recent trends, Materials 13 (2020) 1411, https://doi.org/10.3390/ma13061411.

[12] T. Sonar, M. Ivanov, E. Trofimov, A. Tingaev, I. Suleymanova, A comprehensive review on fusion welding of high entropy alloys – processing, microstructural evolution and mechanical properties of joints, Int. J. Light. Mater. Manuf. 7 (2024) 122–183, https://doi.org/10.1016/j.ijlmm.2023.06.003.

[13] N. Kashaev, V. Ventzke, N. Stepanov, D. Shaysultanov, V. Sanin, S. Zherebtsov, Laser beam welding of a CoCrFeNiMn-type high entropy alloy produced by self-propagating high-temperature synthesis, Intermetallics 96 (2018) 63–71, https://doi.org/10.1016/j.intermet.2018.02.014.

[14] M.-G. Jo, H.-J. Kim, M. Kang, P.P. Madakashira, E.S. Park, J.-Y. Suh, D.-I. Kim, S.-T. Hong, H.N. Han, Microstructure and mechanical properties of friction stir welded and laser welded high entropy alloy CrMnFeCoNi, Met. Mater. Int. 24 (2018) 73–83, https://doi.org/10.1007/s12540-017-7248-x.

[15] J. Shen, Y.T. Choi, J. Yang, J. He, Z. Zeng, N. Zhou, A.C. Baptista, H.S. Kim, J. P. Oliveira, Fabrication of spatially-variable heterostructured CoCrFeMnNi high entropy alloy by laser processing, Mater. Sci. Eng. A 896 (2024) 146272, https://doi.org/10.1016/j.msea.2024.146272.

[16] J. Shen, R. Gonçalves, Y.T. Choi, J.G. Lopes, J. Yang, N. Schell, H.S. Kim, J. P. Oliveira, Microstructure and mechanical properties of gas metal arc welded CoCrFeMnNi joints using a 410 stainless steel filler metal, Mater. Sci. Eng. A 857 (2022) 144025, https://doi.org/10.1016/j.msea.2022.144025.

[17] N. Kashaev, V. Ventzke, N. Petrov, M. Horstmann, S. Zherebtsov, D. Shaysultanov, V. Sanin, N. Stepanov, Fatigue behaviour of a laser beam welded CoCrFeNiMn-type high entropy alloy, Mater. Sci. Eng. A 766 (2019) 138358, https://doi.org/10.1016/j.msea.2019.138358.

[18] Z. Wu, S.A. David, D.N. Leonard, Z. Feng, H. Bei, Microstructures and mechanical properties of a welded CoCrFeMnNi high-entropy alloy, Sci. Technol. Weld. Join. 23 (2018) 585–595, https://doi.org/10.1080/13621718.2018.1430114.

[19] S. Park, H. Nam, J. Park, Y. Na, H. Kim, N. Kang, Superior-tensile property of CoCrFeMnNi alloys achieved using friction-stir welding for cryogenic applications, Mater. Sci. Eng. A 788 (2020) 139547, https://doi.org/10.1016/j.msea.2020.139547.

[20] H. Nam, S. Park, S.-W. Kim, S.H. Shim, Y. Na, N. Kim, S. Song, S.I. Hong, N. Kang, Enhancement of tensile properties applying phase separation with Cu addition in gas tungsten arc welds of CoCrFeMnNi high entropy alloys, Scr. Mater. 220 (2022) 114897, https://doi.org/10.1016/j.scriptamat.2022.114897.

[21] J.-Y. Lin, Z.-H. Lai, T. Otsuki, H.-W. Yen, S. Nambu, Gradient microstructure and interfacial strength of CoCrFeMnNi high-entropy alloy in solid-state ultrasonic welding, Mater. Sci. Eng. A 825 (2021) 141885, https://doi.org/10.1016/j.msea.2021.141885.

[22] Z. Chen, B. Wang, B. Duan, X. Zhang, Mechanical properties and microstructure of laser welded FeCoNiCrMn high-entropy alloy, Mater. Lett. 262 (2020) 127060, https://doi.org/10.1016/j.matlet.2019.127060.

[23] J. Shen, Y. Taek Choi, R. Gonçalves, N. Schell, J. Yang, Z. Zeng, A. Catarina Baptista, H. Seop Kim, J.P. Oliveira, Synergistic effects of Monel 400 filler wire in gas metal arc welding of CoCrFeMnNi high entropy alloy, Mater. Des. 242 (2024) 112996, https://doi.org/10.1016/j.matdes.2024.112996.

[24] P. Zhang, Y. Qi, Q. Cheng, X. Sun, Welding dissimilar alloys of CoCrFeMnNi high-entropy alloy and 304 stainless steel using gas Tungsten Arc Welding, J. Mater. Eng. Perform. 33 (2024) 3273–3282, https://doi.org/10.1007/s11665-023-08229-1.

[25] H. Yao, K. Chen, K. Kondoh, X. Dong, M. Wang, X. Hua, A. Shan, Microstructure and mechanical properties of friction stir lap welds between FeCoCrNiMn high entropy alloy and 6061 Al alloy, Mater. Des. 224 (2022) 111411, https://doi.org/10.1016/j.matdes.2022.111411.

[26] M. Rhode, K. Erxleben, T. Richter, D. Schroepfer, T. Mente, T. Michael, Local mechanical properties of dissimilar metal TIG welded joints of CoCrFeMnNi high entropy alloy and AISI 304 austenitic steel, Weld. World 68 (2024) 1563–1573, https://doi.org/10.1007/s40194-024-01718-4.

[27] D. Afonso, J.G. Lopes, Y.T. Choi, R.E. Kim, N. Schell, N. Zhou, H.S. Kim, J. P. Oliveira, Dissimilar laser welding of an as-rolled CoCrFeMnNi high entropy alloy to Inconel 718 superalloy, Opt Laser. Technol. 180 (2024) 111427, https://doi.org/10.1016/j.optlastec.2024.111427.

[28] K. Ziewiec, A. Błachowski, S. Kąc, A. Ziewiec, Formation, microstructure, and properties of dissimilar welded joint between CrMnFeCoNi and Fe, Materials 16 (2023) 5187, https://doi.org/10.3390/ma16145187.

[29] R.H. Buzolin, T. Richter, F. Pixner, M. Rhode, D. Schroepfer, N. Enzinger, Microstructure and texture characterisation of friction stir welded CoCrNi and CoCrFeMnNi multi-principle element alloys, Mater. Today Commun. 35 (2023) 105870, https://doi.org/10.1016/j.mtcomm.2023.105870.

[30] H. Nam, B. Moon, S. Park, N. Kim, S. Song, N. Park, Y. Na, N. Kang, Gas tungsten arc weldability of stainless steel 304 using CoCrFeMnNi filler metals for cryogenic applications, Sci. Technol. Weld. Join. 27 (2022) 33–42, https://doi.org/10.1080/13621718.2021.1996851.

[31] J.P. Oliveira, A. Shamsolhodaei, J. Shen, J.G. Lopes, R.M. Gonçalves, M. de Brito Ferraz, L. Piçarra, Z. Zeng, N. Schell, N. Zhou, H. Seop Kim, Improving the ductility in laser welded joints of CoCrFeMnNi high entropy alloy to 316 stainless steel, Mater. Des. 219 (2022) 110717, https://doi.org/10.1016/j.matdes.2022.110717.

[32] R.H. Buzolin, T. Richter, F. Pixner, M. Rhode, D. Schroepfer, N. Enzinger, Microstructure and texture characterisation of friction stir welded CoCrNi and CoCrFeMnNi multi-principle element alloys, Mater. Today Commun. 35 (2023) 105870, https://doi.org/10.1016/j.mtcomm.2023.105870.

[33] J. Wang, F. Peng, L. Zhou, Y. Luo, W. Zhang, Z. Wu, High-strength ductility joining of multicomponent alloy to 304 stainless steel using laser welding technique, Materials 16 (2023) 2374, https://doi.org/10.3390/ma16062374.

[34] H. Do, S. Asadi, N. Park, Microstructural and mechanical properties of dissimilar friction stir welded CoCrFeMnNi high entropy alloy to STS304 stainless steel, Mater. Sci. Eng. A 840 (2022) 142979, https://doi.org/10.1016/j.msea.2022.142979.

[35] G. Wang, G. Sheng, J. Sun, Y. Wei, X. Gao, Z. Yu, X. Yuan, Mechanical properties and microstructure evolution of CrMnFeCoNi HEA/304 SS dissimilar brazing joints, J. Alloys Compd. 829 (2020) 154520, https://doi.org/10.1016/j.jallcom.2020.154520.

[36] N.K. Adomako, J.H. Kim, Microstructure and mechanical properties of dissimilar laser lap joint between CoCrFeMnNi-high entropy alloy and duplex stainless steel, Mater. Lett. 288 (2021) 129354, https://doi.org/10.1016/j.matlet.2021.129354.

[37] J.P. Oliveira, J. Shen, Z. Zeng, J.M. Park, Y.T. Choi, N. Schell, E. Maawad, N. Zhou, H.S. Kim, Dissimilar laser welding of a CoCrFeMnNi high entropy alloy to 316 stainless steel, Scr. Mater. 206 (2022) 114219, https://doi.org/10.1016/j.scriptamat.2021.114219.

[38] H. Nam, S. Park, E.-J. Chun, H. Kim, Y. Na, N. Kang, Laser dissimilar weldability of cast and rolled CoCrFeMnNi high-entropy alloys for cryogenic applications, Sci. Technol. Weld. Join. 25 (2020) 127–134, https://doi.org/10.1080/13621718.2019.1644471.

[39] N.K. Adomako, G. Shin, N. Park, K. Park, J.H. Kim, Laser dissimilar welding of CoCrFeMnNi-high entropy alloy and duplex stainless steel, J. Mater. Sci. Technol. 85 (2021) 95–105, https://doi.org/10.1016/j.jmst.2021.02.003.

[40] H. Nam, S. Yoo, J. Lee, Y. Na, N. Park, N. Kang, GTA weldability of rolled high-entropy alloys using various filler metals, Metals 10 (2020) 1371, https://doi.org/10.3390/met10101371.

[41] J. Xin, W. Wang, X. Yang, M. Boubeche, S. Wang, H. Zhang, C. Huang, Y. Li, B. Lyu, F. Shen, W. Sun, L. Li, Dissimilar laser welding of CrMnFeCoNi high entropy alloy and 316LN stainless steel for cryogenic application, J. Mater. Sci. Technol. 163 (2023) 158–167, https://doi.org/10.1016/j.jmst.2023.04.030.

[42] C.-C. Hsieh, W. Wu, Overview of intermetallic sigma %28%29 phase precipitation in stainless steels, ISRN Metall. 2012 (2012) 1–16, https://doi.org/10.5402/2012/732471.

[43] J.-H. Yoon, E.-P. Yoon, B.-S. Lee, Correlation of chemistry, microstructure and ductile fracture behaviours of niobium-stabilized austenitic stainless steel at elevated temperature, Scr. Mater. 57 (2007) 25–28, https://doi.org/10.1016/j.scriptamat.2007.03.025.

[44] J. Erneman, M. Schwind, H. Andren, J. Nilsson, A. Wilson, J. Agren, The evolution of primary and secondary niobium carbonitrides in AISI 347 stainless steel during manufacturing and long-term ageing, Acta Mater. 54 (2005) 67–76, https://doi.org/10.1016/j.actamat.2005.08.028.

[45] J. Erneman, M. Schwind, P. Liu, J.-O. Nilsson, H.-O. Andrén, J. Ågren, Precipitation reactions caused by nitrogen uptake during service at high temperatures of a niobium stabilised austenitic stainless steel, Acta Mater. 52 (2004) 4337–4350, https://doi.org/10.1016/j.actamat.2004.06.001.

[46] L. Singhal, J. Martin, The formation of ferrite and sigma-phase in some austenitic stainless steels, Acta Metall. 16 (1968) 1441–1451, https://doi.org/10.1016/0001-6160(68)90039-4.

[47] J. Barcik, The kinetics of σ-phase precipitation in AISI310 and AISI316 steels, Metall. Trans. A 14 (1983) 635–641, https://doi.org/10.1007/BF02643779.

[48] L.H. Guilherme, A.V. Benedetti, C.S. Fugivara, R. Magnabosco, M.F. Oliveira, Effect of MAG welding transfer mode on sigma phase precipitation and corrosion performance of 316L stainless steel multi-pass welds, J. Mater. Res. Technol. 9 (2020) 10537–10549, https://doi.org/10.1016/j.jmrt.2020.07.039.

[49] N.K. Adomako, G. Shin, N. Park, K. Park, J.H. Kim, Laser dissimilar welding of CoCrFeMnNi-high entropy alloy and duplex stainless steel, J. Mater. Sci. Technol. 85 (2021) 95–105, https://doi.org/10.1016/j.jmst.2021.02.003.

[50] Y.-K. Kim, Y.-A. Joo, H.S. Kim, K.-A. Lee, High temperature oxidation behavior of Cr-Mn-Fe-Co-Ni high entropy alloy, Intermetallics 98 (2018) 45–53, https://doi.org/10.1016/j.intermet.2018.04.006.

[51] U. Gürol, M. Tümer, S. Dilibal, Experimental investigation of wire arc additively manufactured inconel 625 superalloy, Trans. Indian Inst. Met. 76 (2023) 1371–1379, https://doi.org/10.1007/s12666-022-02797-x.

[52] Z. Li, Interstitial equiatomic CoCrFeMnNi high-entropy alloys: carbon content, microstructure, and compositional homogeneity effects on deformation behavior, Acta Mater. 164 (2019) 400–412, https://doi.org/10.1016/j.actamat.2018.10.050.

[53] J.P. Oliveira, A. Shamsolhodaei, J. Shen, J.G. Lopes, R.M. Gonçalves, M. de Brito Ferraz, L. Piçarra, Z. Zeng, N. Schell, N. Zhou, H. Seop Kim, Improving the ductility in laser welded joints of CoCrFeMnNi high entropy alloy to 316 stainless steel, Mater. Des. 219 (2022) 110717, https://doi.org/10.1016/j.matdes.2022.110717.